Supporting Information

Si-Substituted MAX Phases and *In-Situ* Formation of Si-Coated MXene Composites via Chlorosilane Etching

Xudong Wang [a,b,c], *Qian Fang* [a,b,c], *Mian Li* [a,c], *Zhifang Chai* [a,c], *Qing Huang* [b,c,*]

[a] Zhejiang Key Laboratory of Data-Driven High-Safety Energy Materials and Applications, Ningbo Key Laboratory of Special Energy Materials and Chemistry, Ningbo Institute of Materials Technology and Engineering, Chinese Academy of Sciences, Ningbo, 315201, China.

[b] University of Chinese Academy of Sciences, Beijing, 100049, China.

[c] Qianwan Institute of CNiTECH, Ningbo 315336, China.

* Corresponding authors.

E-mail address: huangqing@nimte.ac.cn (Qing Huang).

MATERIALS AND METHODS

Materials

Ti powder (300 mesh, 99.9%), Nb powder (300 mesh, 99.9%), Ta powder (300 mesh, 99.9%), V powder (300 mesh, 99.9%), Cr powder (300 mesh, 99.9%), graphite (500 nm, 99.9%), TiN powder (300 mesh, 99.9%) were purchased from Aladdin. $ZnCl_2$ (99.5%), Al powder (10-20 μm, 99.9%) were purchased from Sinopharm Chemical Reagent Co., Ltd.. $SiCl_4$ (50 ml, 99.5%) were purchased from Macklin.

Preparation of Precursor MAX Phases

Ti_2AlC, Ti_3AlC_2, Ti_2AlN, Nb_2AlC, Ta_2AlC, V_2AlC, Cr_2AlC, Ta_4AlC_3, Nb_2ZnC were synthesized as previously reported.[1-9]

Preparation of Si-Substituted MAX Phases

All Si-substituted MAX phases were synthesized by exposing the precursors to $SiCl_4$ vapor. Specifically, approximately 0.5 g of pre-synthesized Al-MAX phase precursor was loaded into a quartz tube. Corresponding volumes of $SiCl_4$ liquid were carefully dispensed using a micropipette in an inert glove box according to the stoichiometric ratios listed in **Table S1**. The quartz tube was then sealed under vacuum using a tube-sealing system. During the sealing process, liquid nitrogen was applied to the bottom of the tube to freeze the $SiCl_4$, thereby preventing its evaporation under vacuum or during high-temperature sealing. The sealed quartz tube was heated at a specified temperature for a predetermined duration. After cooling, the obtained product was washed with ethanol or deionized water to thoroughly remove volatile $AlCl_3$, producing the final product for subsequent characterization.

Preparation of *In-Situ* Si-Coated MXene Composites

The start materials of Ti_2AlC/Ti_3AlC_2 and $SiCl_4$ (stoichiometrically proportioned per **Table S1**) was sealed in an evacuated quartz tube under liquid nitrogen cooling to prevent $SiCl_4$ volatilization. The tube was then heated in a muffle furnace at designated temperatures and durations, producing the *in-situ* Si-coated MXene composite after cooling.

Characterization Methods

Phase identification and structural analysis were performed using X-ray diffraction

(XRD; Bruker D8 Advance, Germany, Cu Kα radiation, λ = 1.5406 Å) operated at 40 kV and 40 mA. Data were collected in the 2θ range of 5 - 80° with a step size of 0.02°. The lattice parameters, atomic coordinates and site occupancies of the series of Si-substituted MAX phases were calculated and verified by the Rietveld method using the software of *TOPAS-Academic v6*. The results are summarized in **Table S2**. Microstructural and elemental analyses were conducted using a field-emission scanning electron microscope (SEM; Hitachi Regulus 8230, Japan) equipped with an EDS detector. Samples were dispersed on conductive carbon tape prior to imaging. Point analyses were performed to confirm atomic ratios. For the EDS evidence regarding the A-site occupancy of Si mentioned in the text, measurements were taken from at least three different points and averaged to calculate the occupancy of Si at the A-site (**Table S3**). Atomic-resolution structural and chemical analysis was performed using aberration-corrected high-angle annular dark-field scanning transmission electron microscopy (HAADF-STEM; Spectra 300, USA). Thin foils were prepared by focused ion beam (FIB; Thermo Scientific Helios-G4-CX, USA) technique. EPR measurements were carried out at room temperature using a Bruker E500 spectrometer to detect unpaired electrons associated with Si vacancies. X-ray photoelectron spectra (XPS) were recorded in an XPS system (Axis Ultra DLD, Kratos, U.K.) with a monochromatic Al X-ray source. The binding energy (BE) scale for charge correction was assigned by adjusting the C 1s peak at 284.8 eV.

Calculation of Redox Potentials

In previous studies, the A-site elements in MAX phases were modeled as metallic species. The Gibbs free energy of reactions between various molten salts and these A-site elements was calculated using HSC software (version 6.0) to predict their reactivity.[10] In this model, the A-site element is typically assigned an oxidation state of approximately zero. This assignment is reasonable because the M-site transition metals, with their lower electronegativity, tend to donate electrons to the more electronegative X-site atoms.[11] Moreover, the transformation between MAX phases typically involves only the oxidation of the A-site element and the insertion of a new A-element. In contrast, MXene formation requires additional oxidation of the M-site

elements to higher oxidation states.[9,12] Following a similar formal oxidation state approach (as seen in binary carbides like TiC, where Ti and C are assigned +4 and -4 states, respectively), we assigned the M element a +2 oxidation state in MAX phases and a +3 state in their derived MXenes. Based on this assignment, the redox potential (V vs. Cl_2/Cl^-) of the M^{3+}/M^{2+} couple was calculated using the HSC software (version 6.0).

The Gibbs free energy change (ΔG_r) for reactions (1) to (3) was calculated using HSC Chemistry software (version 6.0).

$$MCl_3\,(s) = MCl_2\,(s) + 1/2\ Cl_2\,(g) \qquad \Delta G_r \qquad (1)$$

$$SiCl_4\,(g) = Si\,(s) + 2\ Cl_2\,(g) \qquad \Delta G_r \qquad (2)$$

$$ACl_n\,(g/s) = A\,(s) + n/2\ Cl_2\,(g) \qquad \Delta G_r \qquad (3)$$

The redox potential (E, in volts vs. Cl_2/Cl^-) was determined from its corresponding Gibbs free energy change in a temperature range of 600-800 ℃ using the fundamental relationship:

$$E(V) = -\frac{\Delta Gr}{nF}$$

where ΔGr is the Gibbs free energy per mole of reaction (in J mol^{-1}), n is the number of electrons transferred and F is the Faraday constant (96485 C mol^{-1}). All the potential values are shown in **Table S5** and **Fig. 5a**.

Corrosion resistance tests

Sample preparation: Approximately 200 mg of each MAX phase powder was accurately weighed using an analytical balance (Mettler Toledo, precision: ±0.01 mg) and placed in polyethylene centrifuge tubes.

Two corrosive solutions were prepared: (i) 1 M NaOH (alkaline medium) and (ii) 6 M HCl (acidic medium). Both solutions were freshly prepared using deionized water (18.2 MΩ·cm) and analytical grade reagents.

Immersion procedure: 50 mL of the corrosive solution was added to each tube containing the MAX phase powder. The tubes were sealed and maintained at 30 °C in a thermostatic water bath without agitation. Immersion durations were set at 6 hours, and 2, 4, 6, and 10 days. For each time point, separate samples were used to avoid

repeated sampling from the same batch.

Post-immersion treatment: After the designated immersion time, the suspensions were centrifuged at 8000 rpm for 5 minutes to separate the powder from the corrosive solution. The supernatant was carefully discarded, and the collected powder was re-dispersed in 50 mL of deionized water. This washing process was repeated three times with deionized water, followed by two additional washing cycles with ethanol to remove residual corrosion products and salts. After the final centrifugation, the washed powders were collected and dried in a vacuum oven at 30 °C for 12 h.

Characterization and analysis: The corrosion behavior was assessed using multiple techniques:

(1) Mass change measurement: The dried samples were re-weighed, and the mass change rate was calculated as:

$$\Delta m\ (\%) = [(m_t - m_0)/m_0] * 100\%$$

where m_0 is the initial mass and m_t is the mass after immersion. Measurements were performed in triplicate, and the average values with standard deviations are reported.

(2) Phase analysis: XRD patterns of the samples before and after immersion were collected to identify any corrosion-induced phase transformations or the formation of secondary phases.

(3) Morphological and elemental analysis: SEM was used to examine surface morphological changes, and EDS was employed to determine the elemental composition of corrosion products.

(4) Kinetic analysis: The segmental mass change rate for each immersion interval was calculated to evaluate the corrosion kinetics. The corrosion rate (R, % per day) for each interval was determined as $R = \Delta m/\Delta t$, where Δm is the mass change during the interval and Δt is the interval duration in days.

Table S1. Reaction conditions between precursors and chlorosilane

Target phases	Starting materials			Temp. (°C), Time (h)
	Parent phases	Chlorosilanes	Mole ratio	
Ti_2SiC	Ti_2AlC	$SiCl_4$	8:7	700, 8
Ti_2SiN	Ti_2AlN	$SiCl_4$	4:3	700, 8
V_2SiC	V_2AlC	$SiCl_4$	4:3	800, 8
Nb_2SiC	Nb_2AlC	$SiCl_4$	4:3	800, 8
Nb_2SiC	Nb_2AlC	$SiCl_4$	4:1.5	800, 8
Ta_2SiC	Ta_2AlC	$SiCl_4$	4:3	800, 16
Ta_4SiC_3	Ta_4AlC_3	$SiCl_4$	4:3	800, 16
Cr_2SiC	Cr_2AlC	$SiCl_4$	4:3	600, 8
$Nb_2Si_{1/2}C$	Nb_2ZnC	$SiCl_4$	2:1	800, 8
Ti_2CCl_2/Si	Ti_2AlC	$SiCl_4$	4:5	700, 4
$Ti_3C_2Cl_2$/Si	Ti_3AlC_2	$SiCl_4$	4:5	700, 4

Table S2. Lattice parameters and atomic sites of Si-substituted MAX phases determined by Rietveld refinement using the software of *TOPAS-Academic v6*.

MAX Phases	Lattice constants		Equivalent position			R_{wp}[a]	Ref.
	a (Å)	*c* (Å)	M (4f)	Si (2d)	C/N (2a)		
Ti_2SiC	3.047	12.804	(1/3, 2/3, 0.0938)	(1/3, 2/3, 3/4)	(0, 0, 0)	14.09 %	This work
	3.035	12.803	(1/3, 2/3, 0.0920)	(1/3, 2/3, 3/4)	(0, 0, 0)	N/A	Theo.[13]
Ti_2SiN	2.982	13.016	(1/3, 2/3, 0.0874)	(1/3, 2/3, 3/4)	(0, 0, 0)	14.67 %	This work
	2.992	12.779	(1/3, 2/3, 0.093)	(1/3, 2/3, 3/4)	(0, 0, 0)	N/A	Theo.[14]
V_2SiC	2.952	12.104	(1/3, 2/3, 0.0921)	(1/3, 2/3, 3/4)	(0, 0, 0)	12.44 %	This work
	2.917	12.055	(1/3, 2/3, 0.0916)	(1/3, 2/3, 3/4)	(0, 0, 0)	N/A	Theo.[15]
Nb_2SiC	3.196	12.548	(1/3, 2/3, 0.0963)	(1/3, 2/3, 3/4)	(0, 0, 0)	14.03 %	This work

	3.188	12.418	(1/3, 2/3, 0.0971)	(1/3, 2/3, 3/4)	(0, 0, 0)	N/A	Theo.[15]
Ta_2SiC	3.195	12.371	(1/3, 2/3, 0.0958)	(1/3, 2/3, 3/4)	(0, 0, 0)	12.92 %	This work
	3.260	12.420	(1/3, 2/3, 0.0991)	(1/3, 2/3, 3/4)	(0, 0, 0)	N/A	Theo.[15]
Cr_2SiC	2.887	12.041	(1/3, 2/3, 0.0907)	(1/3, 2/3, 3/4)	(0, 0, 0)	12.56 %	This work
	2.841	11.906	(1/3, 2/3, 0.0900)	(1/3, 2/3, 3/4)	(0, 0, 0)	N/A	Theo.[16]
Ta_4SiC_3	3.136	22.562	Ta1(1/3, 2/3, 0.0534); Ta2 (2/3) , 1/3, 0.1628)	(1/3, 2/3, 0.25)	C1 (0, 0, 0); C2 (0, 0, 0.1052)	13.39 %	This work
	3.194	23.729	—	—	—	N/A	Theo.[17]
$Nb_2Si_{1/2}C$	3.456	11.626	(1/3, 2/3, 0.0697)	(1/3, 2/3, 3/4)	(0, 0, 0)	14.89 %	This work

[a] Reliability Factors (R_{wp}) were all below 15 %, indicating a reliable refinement result.

Table S3. Evidence of Si Vacancies at the A-Site in Si-substituted MAX phases: A-Site Si Occupancy from XRD Refinement, M/Si Atomic Ratio via EDS, and Electron Paramagnetic Resonance (EPR).

MAX phases	A-Site Vacancies (V_A) in MAX Phases			
	Occupancy (XRD refinement [a]) / %	Occupancy (EDS) / %	Theoretical Si Occupancy [c]/ %	EPR g-factor
Ti_2SiC	100.0	100.0	100.0	—
Ti_2SiN	77.5	67.3	75.0	—
V_2SiC	91.0	91.0	75.0	—
Nb_2SiC	74.9	72.8	75.0	—
Ta_2SiC	71.4	N/A[b]	75.0	—

Ta_4SiC_3	83.9	N/A[b]	75.0	—
Cr_2SiC	80.0	76.7	75.0	—
$Nb_2Si_{1/2}C$	47.5	56.9	50.0	2.002

[a] Occupancy values were obtained from Rietveld refinement using the software of *TOPAS-Academic v6*. Reliability Factors (R_{wp}) were all below 15 %, indicating a credible and reliable refinement result (Table S2).

[b] The quantification accuracy was compromised due to the overlap of the Ta *M* and Si K_α peaks.

[c] The theoretical Si occupancy was calculated based Equation (5)-(6) and (9)

Table S4. Lattice parameters (*a* and *c*), *z*-coordinate of M (z_M), and the distortion of M_6A trigonal prisms (P_d) for M_2AC MAX phases

MAX Phases	*a* (Å)	*c* (Å)	z_M	P_d	Ref.
Ti_2SiC	3.047	12.804	0.0938	1.143	
Ti_2SiN	2.982	13.016	0.0874	1.093	
V_2SiC	2.952	12.104	0.0921	1.152	
Nb_2SiC	3.196	12.548	0.0963	1.197	This work
Ta_2SiC	3.195	12.371	0.0958	1.204	
Cr_2SiC	2.887	12.041	0.0907	1.136	
$Nb_2Si_{1/2}C$	3.456	11.626	0.0697	1.194	
Ti_2AlC	3.017	13.45	0.0848	1.068	[18]
Ti_2AlN	2.994	13.61	0.0860	1.060	[19]
V_2AlC	2.855	12.992	0.0880	1.067	[20]
Nb_2AlC	3.103	14.032	0.0880	1.072	[20]

Ta_2AlC	3.136	13.999	0.0880	1.080	[20]
Cr_2AlC	2.860	12.820	0.0860	1.069	[21]
Ti_2SC	3.143	11.05	0.0998	1.278	[22]
Nb_2SC	3.31	11.54	0.099	1.279	[23]

Table S5. Redox potentials (V vs. Cl_2/Cl-) of the Si^{4+}/Si, $M^{3+}_{(MXene)}$ /$M^{2+}_{(MAX)}$ and $A^{n+}_{(ACln)}$ /$A_{(MAX)}$ redox couples at 600-800 ℃.

Tem. (℃)	Lewis acid cation	$M^{3+}_{(MXene)}$ /$M^{2+}_{(MAX)}$					$A^{n+}_{(ACln)}$ /$A_{(MAX)}$	
	Si^{4+} /Si	Ti^{3+} /Ti^{2+}	V^{3+}/ V^{2+}	Nb^{3+} /Nb^{2+}	Ta^{3+} /Ta^{2+}	Cr^{3+} /Cr^{2+}	Al^{3+} /Al	Zn^{2+} /Zn
600	-1.418	-1.635	-0.643	-1.092	-0.909	-0.877	-1.869	-1.508
700	-1.385	-1.581	-0.568	-1.014	-0.822	-0.772	-1.850	-1.444
800	-1.351	-1.527	-0.494	-0.937	-0.735	-0.667	-1.827	-1.382

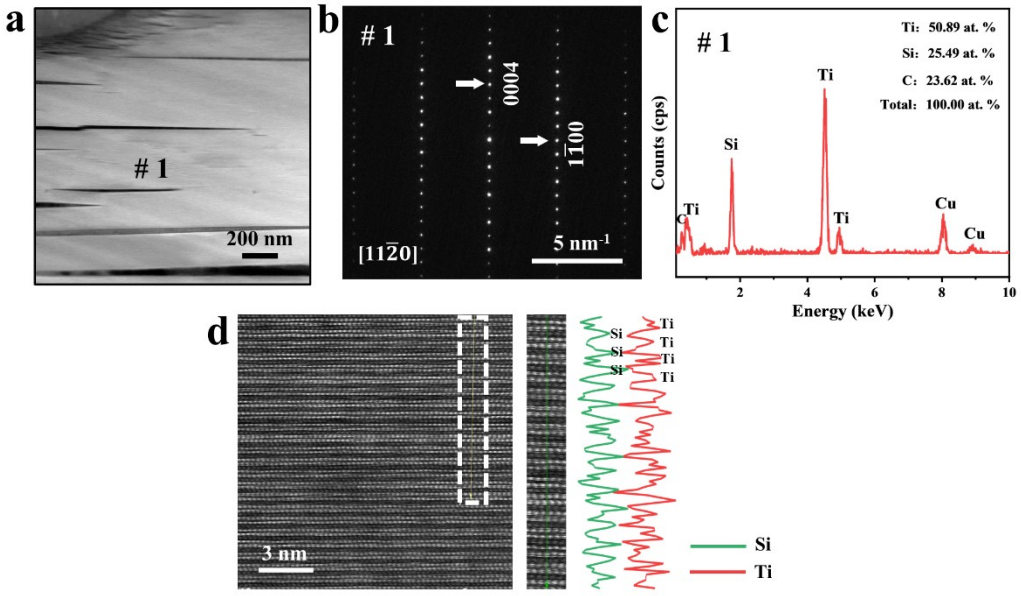

Fig. S1 Structural and compositional analysis of Ti_2SiC by TEM. (a) HAADF-STEM image. (b) Selected-area electron diffraction (SAED) pattern from area #1 in (a), recorded along the [11$\bar{2}$0] zone axis. The (0004) and (1$\bar{1}$00) diffraction spots exhibit a 90° interplanar angle. (c) Energy-dispersive X-ray spectroscopy (EDS) point spectrum acquired from area #1 in (a), confirming a Ti/Si atomic ratio of 2:1. (d) The line-scan energy spectrum at atomic resolution indicates that the brighter dots correspond to Ti, while the darker dots correspond to Si.

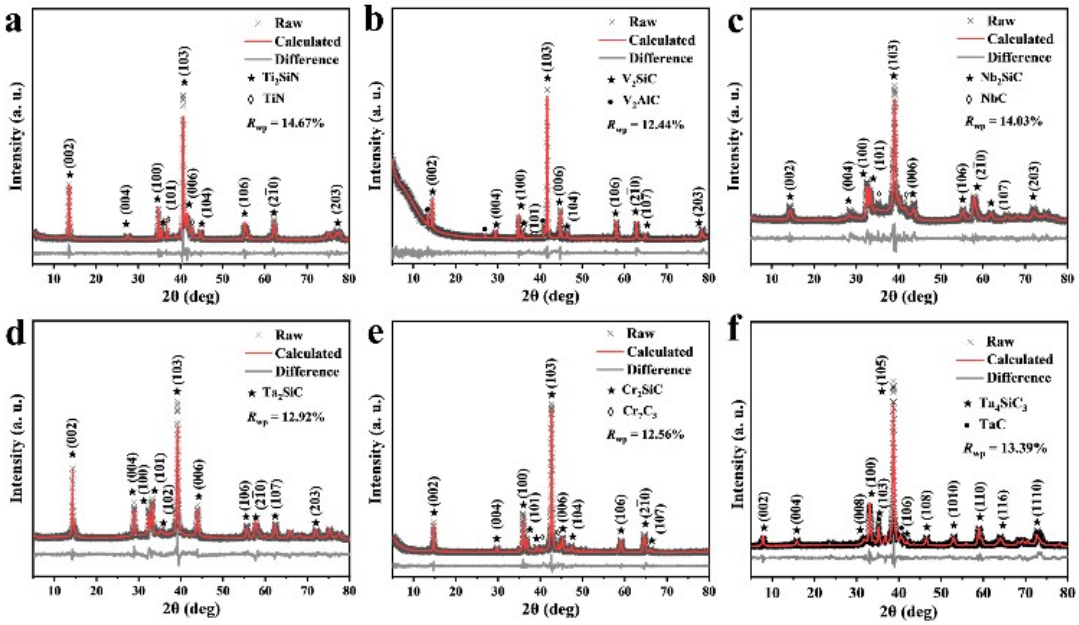

Fig. S2 Rietveld refinement XRD patterns of Si-substituted MAX phases: (a) Ti_2SiN, (b) V_2SiC, (c) Nb_2SiC, (d) Ta_2SiC, (e) Cr_2SiC, and (f) Ta_4SiC_3.

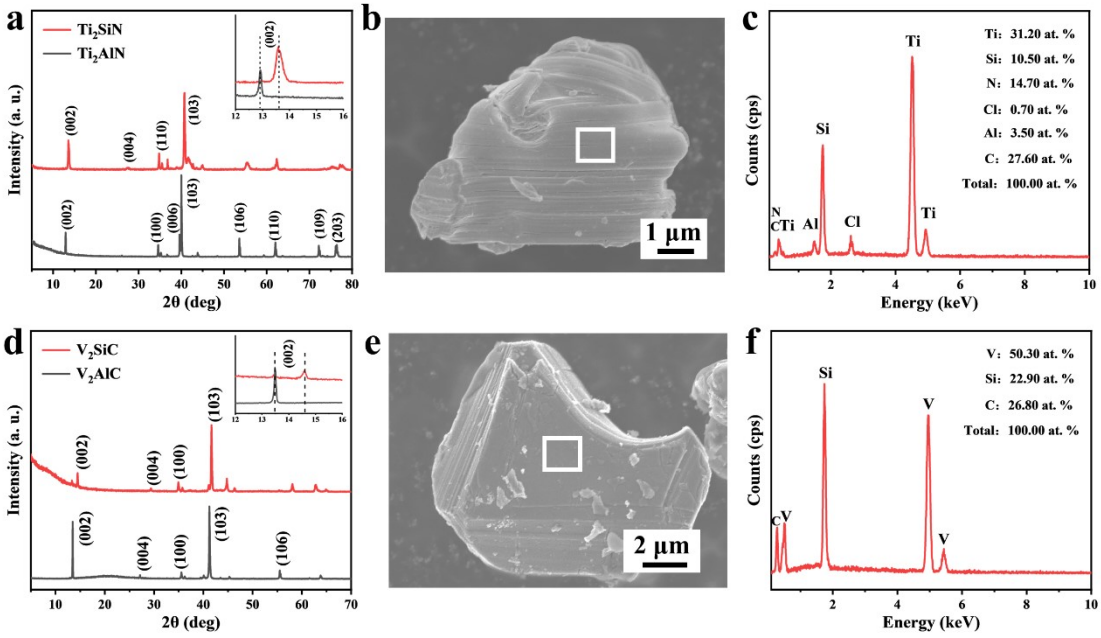

Fig. S3 XRD, Morphology and EDS Analysis of Ti_2SiN and V_2SiC. (a) XRD patterns of Ti_2SiN and its parent phase Ti_2AlN, with partial Miller indices labeled. The inset shows the shift of the (002) peak, indicating a decrease in the *c*-lattice parameter. (b) SEM micrograph of Ti2SiN, revealing a typical layered morphology. (c) EDS analysis of the region highlighted in (b), demonstrating the decrease of Al signals and the emergence of Si signals. (d) XRD patterns of V_2SiC and its parent phase V_2AlC, with partial Miller indices labeled. The inset shows the shift of the (002) peak, indicating a decrease in the *c*-lattice parameter. (e) SEM micrograph of V_2SiC, revealing a typical layered morphology. (f) EDS analysis of the region highlighted in (e), demonstrating the disappearance of Al signals and the emergence of Si signals.

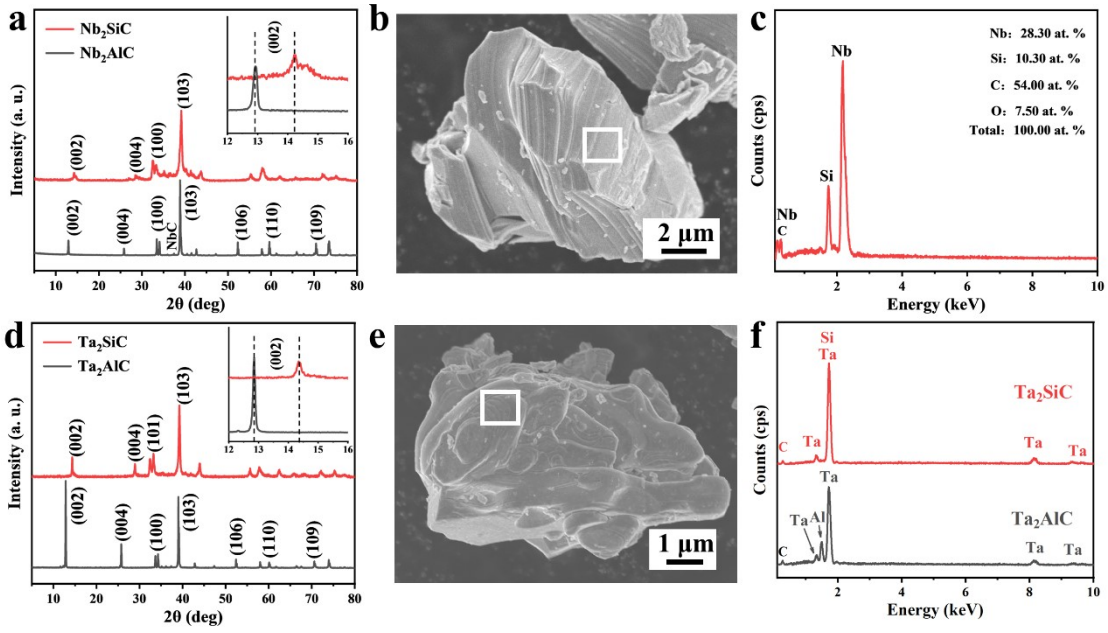

Fig. S4 XRD, Morphology and EDS Analysis of Nb_2SiC and Ta_2SiC. (a) XRD patterns of Nb_2SiC and its parent phase Nb_2AlC, with partial Miller indices labeled. The inset shows the shift of the (002) peak, indicating a decrease in the *c*-lattice parameter. (b) SEM micrograph of Nb_2SiC, revealing a typical layered morphology. (c) EDS analysis of the region highlighted in (b), demonstrating the disappearance of Al signals and the emergence of Si signals. (d) XRD patterns of Ta_2SiC and its parent phase Ta_2AlC, with partial Miller indices labeled. The inset shows the shift of the (002) peak, indicating a decrease in the *c*-lattice parameter. (e) SEM micrograph of Nb_2SiC, revealing a typical layered morphology. (f) EDS analysis of the region highlighted in (e), demonstrating the disappearance of Al signals and the emergence of Si signals.

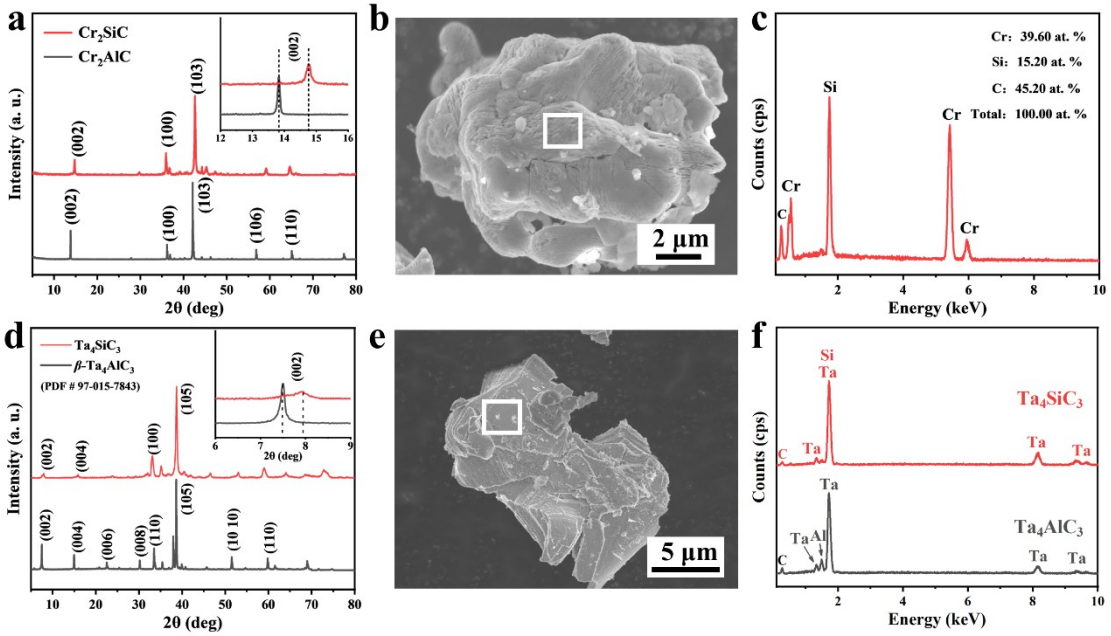

Fig. S5. XRD, Morphology and EDS Analysis of Cr_2SiC and Ta_4SiC_3. (a) XRD patterns of Cr_2SiC and its parent phase Cr_2AlC, with partial Miller indices labeled. The inset shows the shift of the (002) peak, indicating a decrease in the *c*-lattice parameter. (b) SEM micrograph of Cr_2SiC, revealing a typical layered morphology. (c) EDS analysis of the region highlighted in (b), demonstrating the disappearance of Al signals and the emergence of Si signals. (d) XRD patterns of Ta_4SiC_3 and its parent phase Ta_4AlC_3, with partial Miller indices labeled. The inset shows the shift of the (002) peak, indicating a decrease in the *c*-lattice parameter. (e) SEM micrograph of Ta_4SiC_3, revealing a typical layered morphology. (f) EDS analysis of the region highlighted in (e), demonstrating the disappearance of Al signals and the emergence of Si signals.

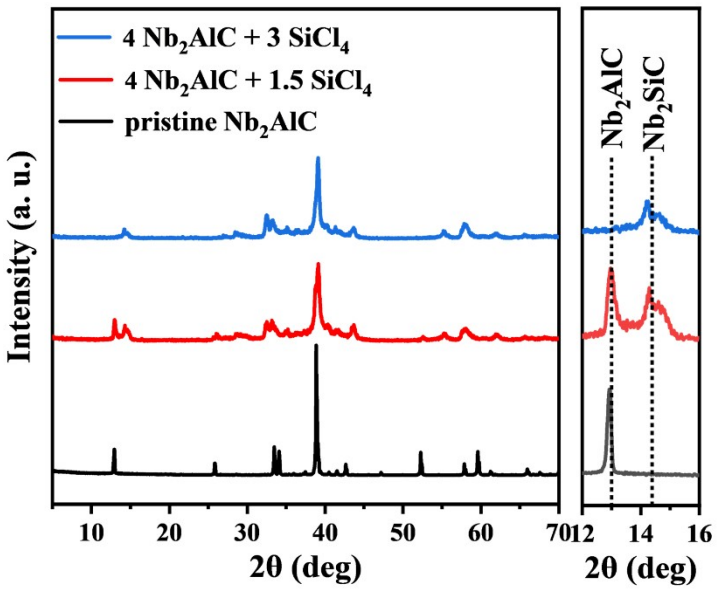

Fig. S6 XRD analysis of products obtained from the reaction of Nb2AlC with varying stoichiometric ratios of SiCl4 at 800 °C for 8 hours.

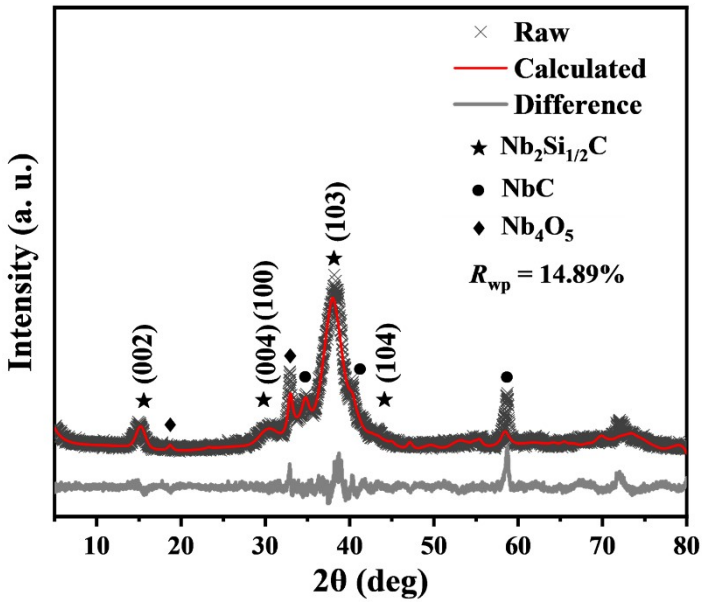

Fig. S7 Rietveld refinement XRD pattern of $Nb_2Si_{1/2}C$, the product of the reaction between Nb_2ZnC and $SiCl_4$ (Equation (6)).

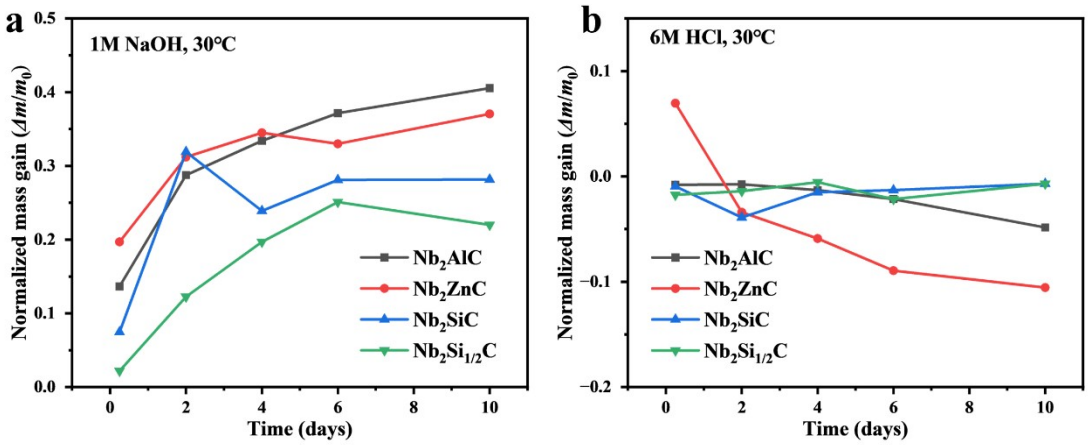

Fig. S8 Mass change of four MAX phases as a function of immersion time in 1 M NaOH (a) and 6 M HCl (b).

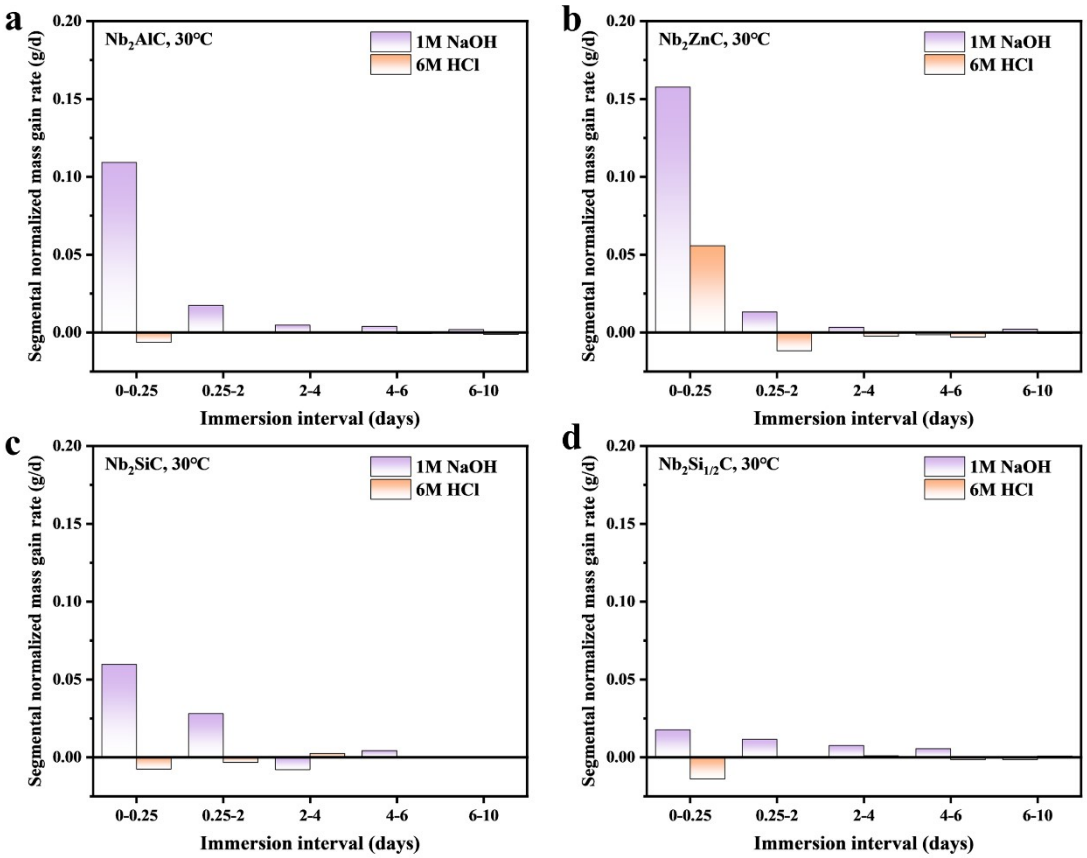

Fig. S9 Segmental mass change rates of four MAX phases over successive immersion intervals in 1 M NaOH and 6 M HCl at 30 °C: (a) Nb_2AlC, (b) Nb_2ZnC, (c) Nb_2SiC, and (d) $Nb_2Si_{1/2}C$.

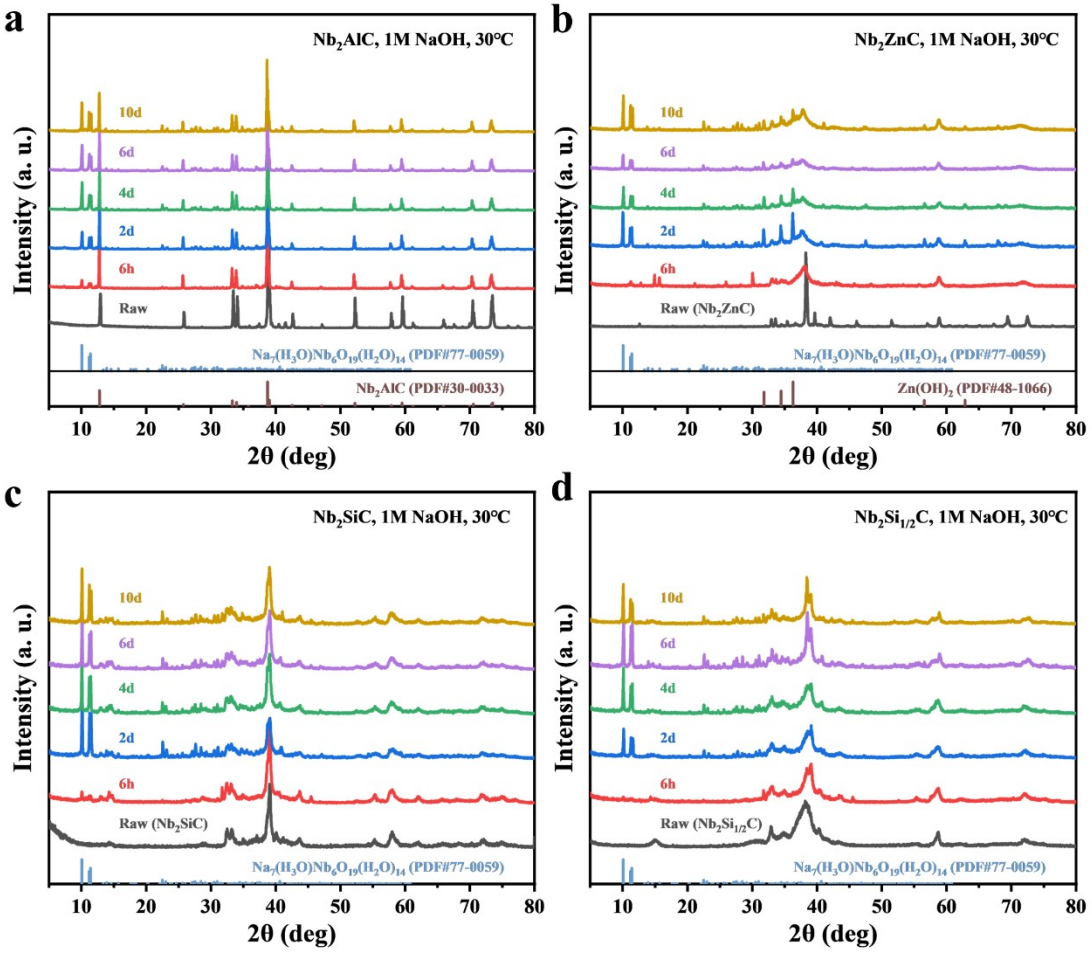

Fig. S10 XRD patterns of four MAX phases after immersion for different durations in 1 M NaOH: (a) Nb_2AlC, (b) Nb_2ZnC, (c) Nb_2SiC, and (d) $Nb_2Si_{1/2}C$.

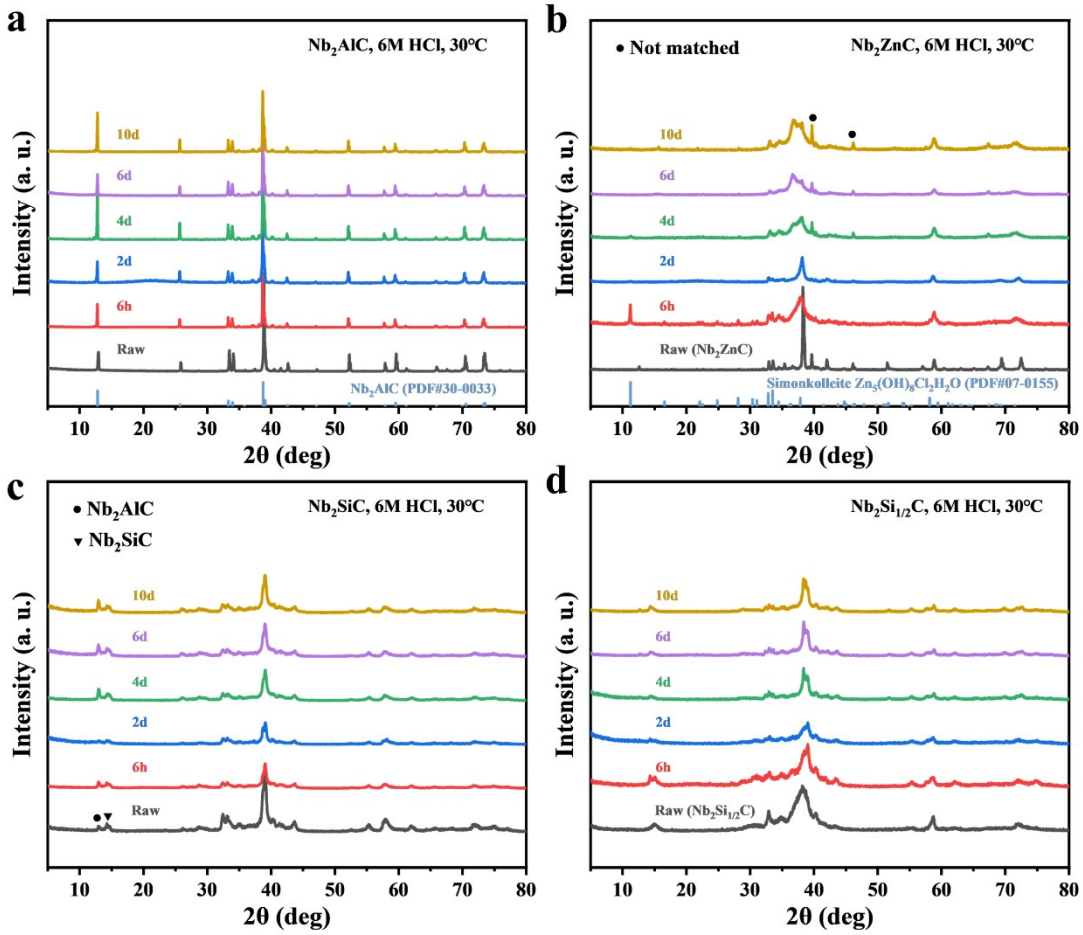

Fig. S11 XRD patterns of four MAX phases after immersion for different durations in 6 M HCl: (a) Nb_2AlC, (b) Nb_2ZnC, (c) Nb_2SiC, and (d) $Nb_2Si_{1/2}C$.

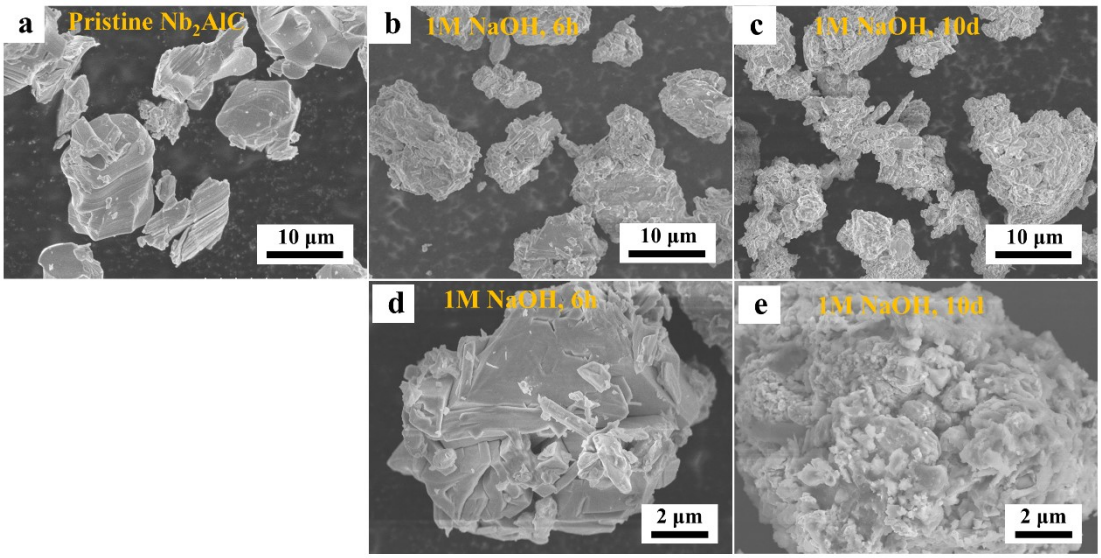

Fig. S12 SEM images of Nb_2AlC before and after immersion in 1 M NaOH: (a) pristine powder; (b, c) low-magnification images after 6 h and 10 d; (d, e) corresponding high-

magnification images.

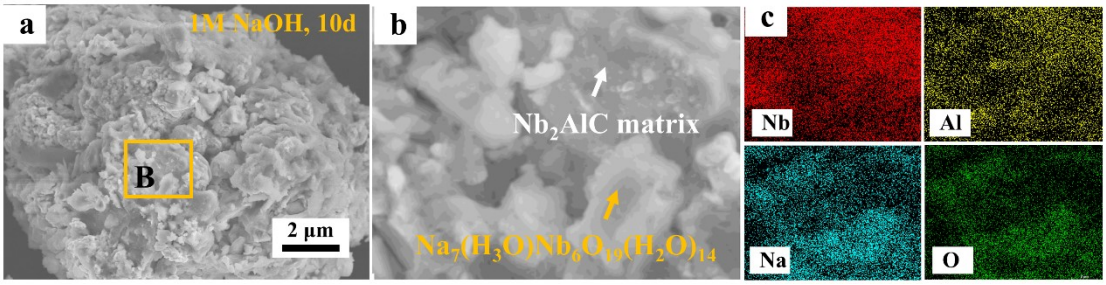

Fig. S13 Morphological and elemental analysis of Nb_2AlC after immersion in 1 M NaOH for 10 days. (a) SEM image showing the overview. (b) Enlarged view of region B in (a). (c) Corresponding EDS elemental maps of region B.

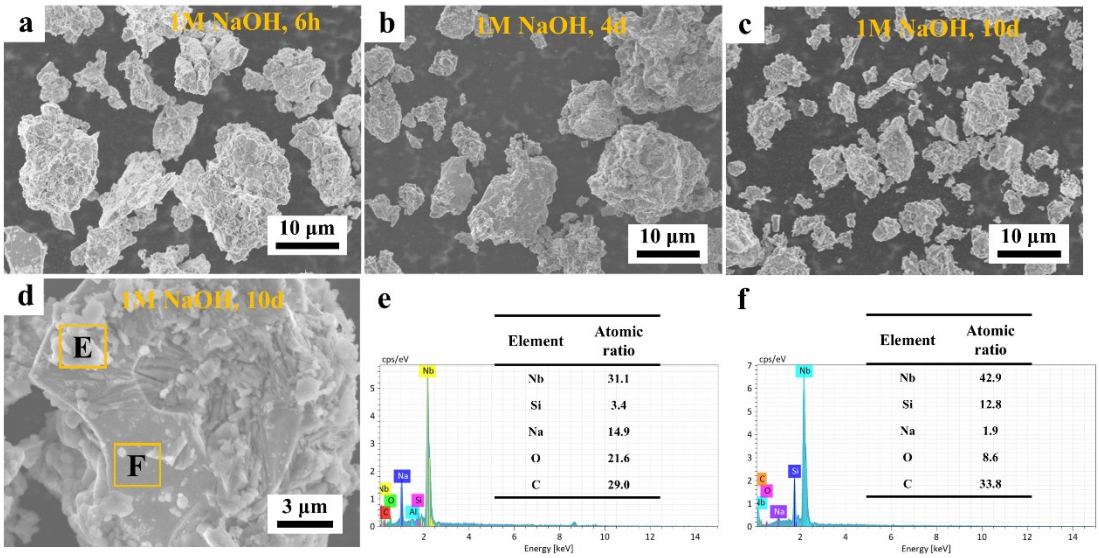

Fig. S14 SEM images of Nb_2SiC after immersion in 1 M NaOH for (a) 6 h, (b) 4 d, and (c) 10 d. (d) High-magnification image of the surface after 10 d. (e, f) EDS spectra acquired from regions E and F in (d), respectively.

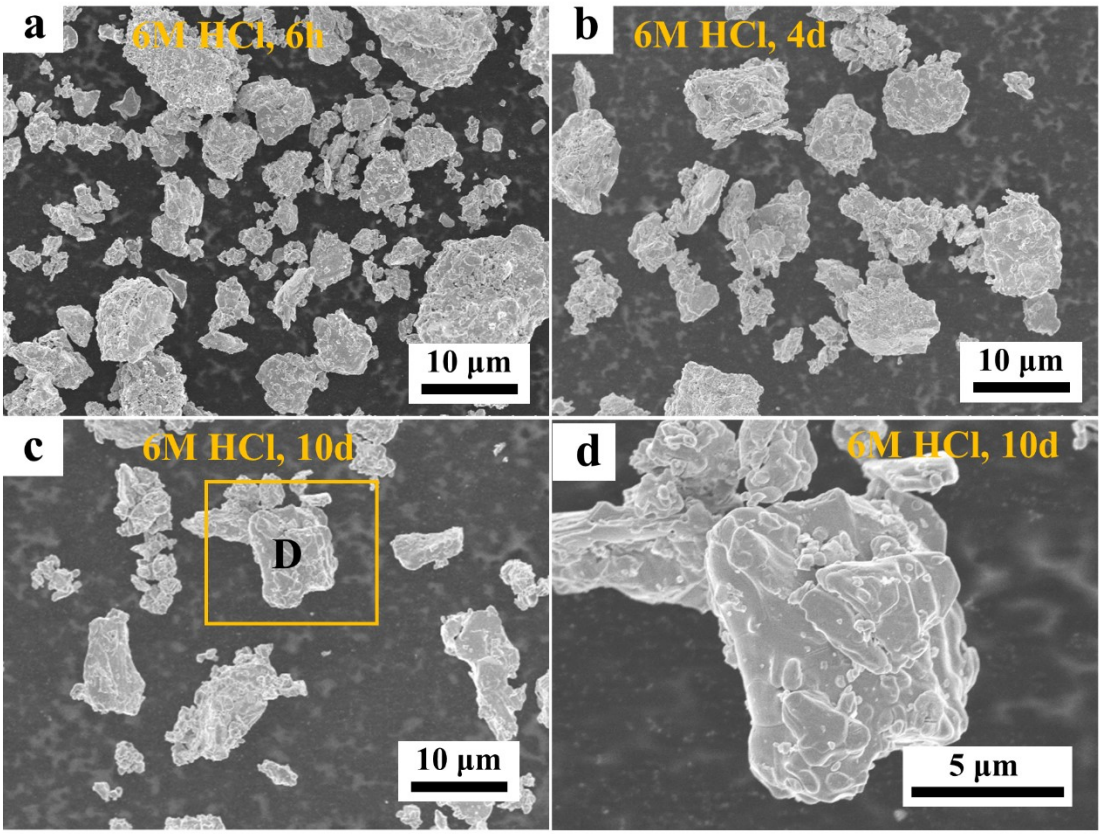

Fig. S15 SEM images of Nb_2AlC before and after immersion in 6 M HCl. (a–c) Low-magnification images after (a) 6 h, (b) 4 d, and (c) 10 d. (d) High-magnification image of region D in (c).

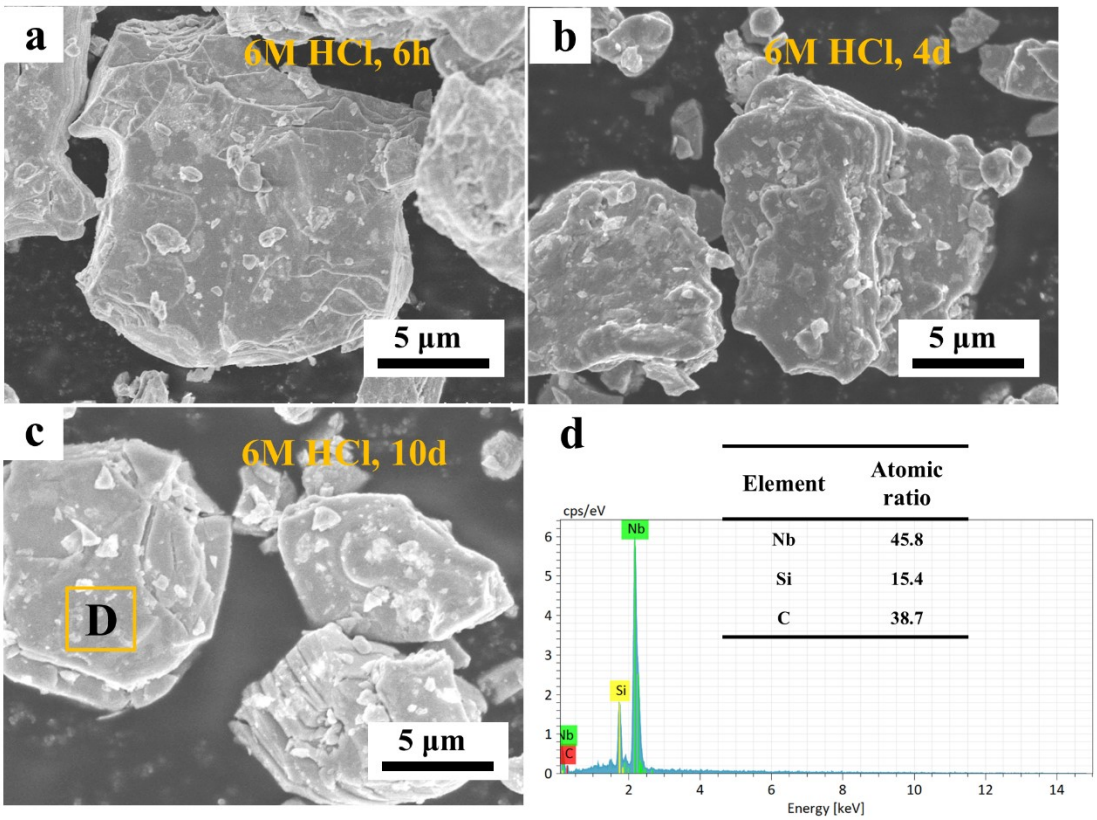

Fig. S16 SEM images of Nb_2SiC after immersion in 6 M HCl for (a) 6 h, (b) 4 d, and (c) 10 d. (d) EDS spectrum acquired from region D in (c).

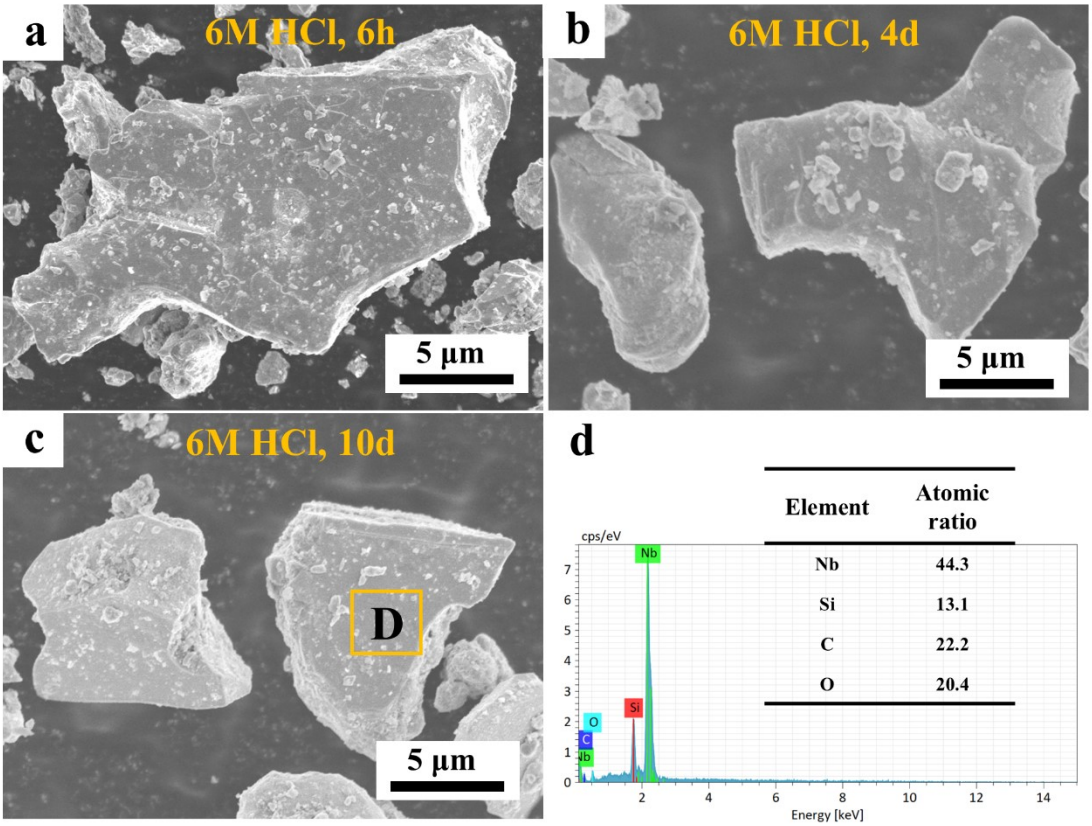

Fig. S17 SEM images of $Nb_2Si_{1/2}C$ after immersion in 6 M HCl for (a) 6 h, (b) 4 d, and (c) 10 d. (d) EDS spectrum acquired from region D in (c).

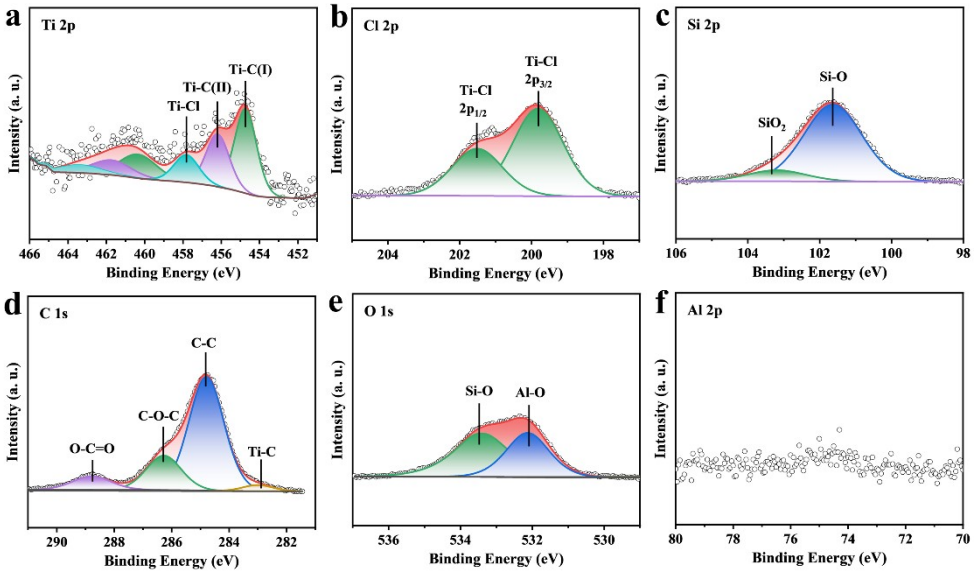

Fig. S18 High-resolution XPS analysis of Si-coated Ti_2CCl_2 composite. (a) The Ti 2p spectrum exhibits peaks at 454.73 eV and 456.19 eV, corresponding to the Ti–C ($2p_{3/2}$) environments [9], and a peak at 457.8 eV is assigned to the Ti–Cl ($2p_{3/2}$) [24]. (b) The Cl 2p spectrum shows a distinct peak at 199.82 eV, further confirming the presence of Ti–Cl ($2p_{3/2}$) [24]. (c) The Si 2p spectrum reveals peaks at 101.63 eV and 103.2 eV, attributable to Si–O and SiO_2 [25]. This superficial oxidation likely occurred on the freshly exposed nano-Si during the $AlCl_3$ removal process. (d) C 1s. (e) O 1s. (f) Al 2p.

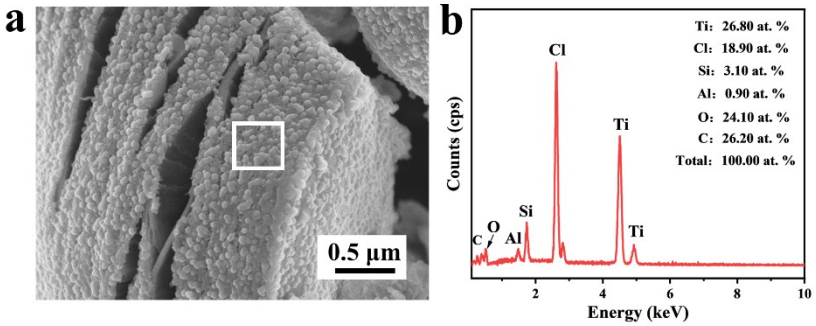

Fig. S19 SEM and EDS analysis of Si-coated Ti_2CCl_2 composite.

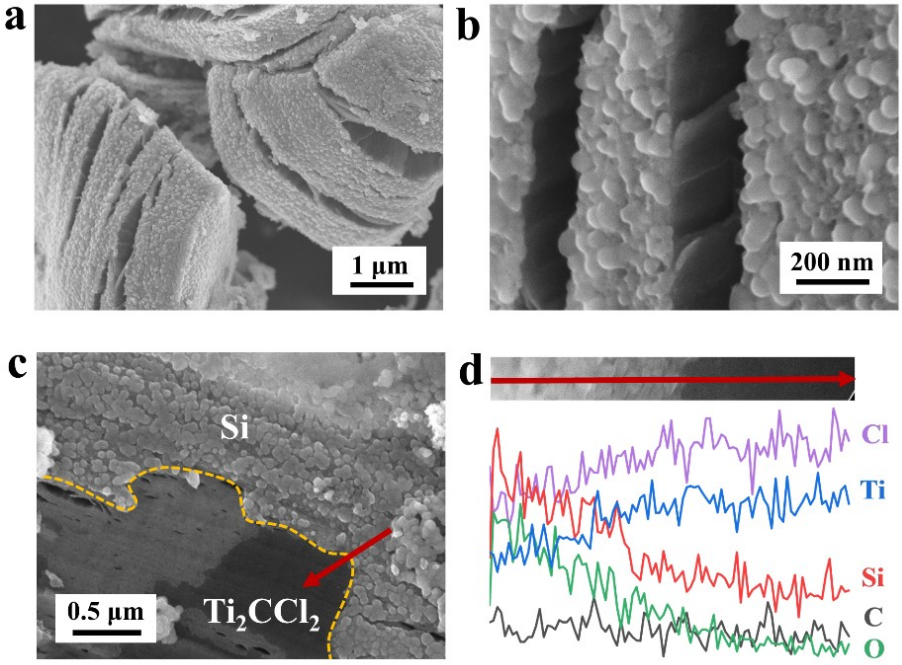

Fig. S20 SEM and EDS analysis of Si-coated Ti_2CCl_2 composite. (a-b) SEM images of Si-coated Ti_2CCl_2 at different magnifications, showing spherical Si particles with diameters around 100 nm. (c) Distinct distribution regions of Ti_2CCl_2 MXene and Si particles. (d) EDS line profile along the red arrow in (c), confirming that the white spherical particles consist of Si.

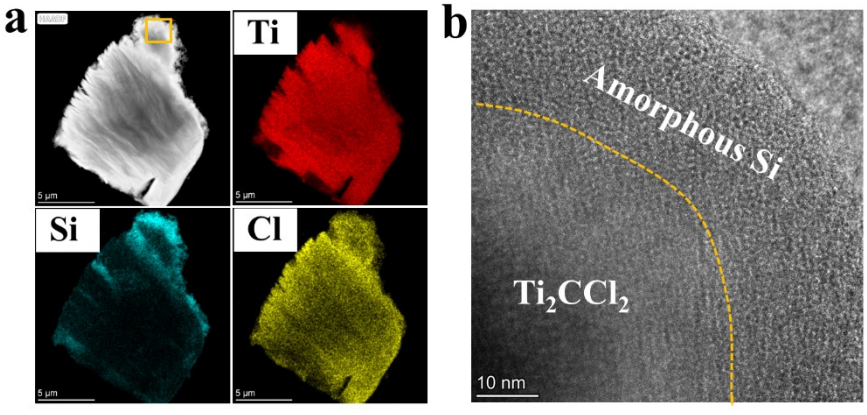

Fig. S21 TEM analysis of Si-coated Ti_2CCl_2. (a) Elements Mapping. (b) HRTEM image of the MXene/Si interface from the area marked in (a).

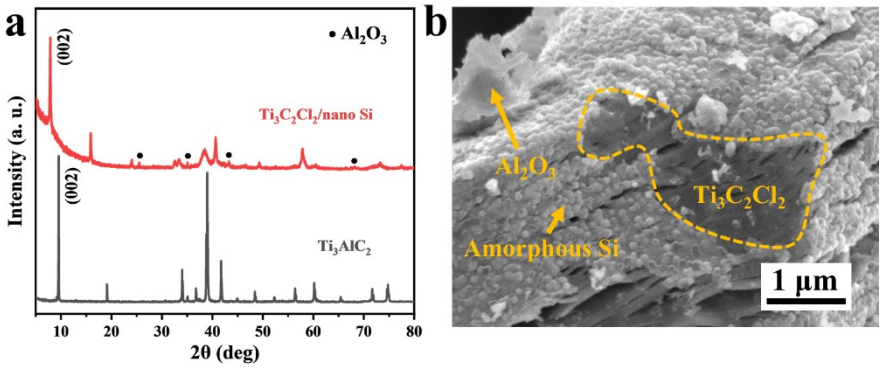

Fig. S22 XRD patterns (a) and SEM image (b) of Si-coated $Ti_3C_2Cl_2$

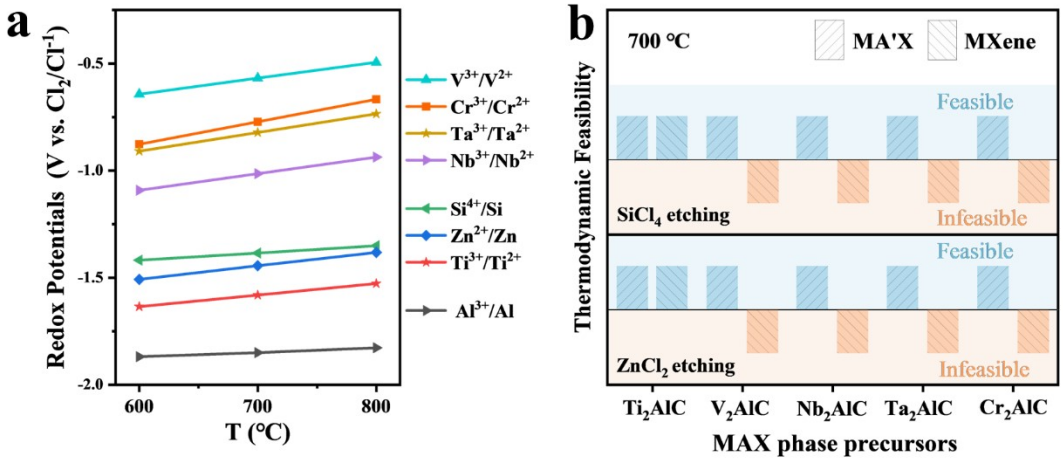

Fig. S23 (a) Redox potentials (V vs. Cl_2/Cl-) of the Si^{4+}/Si, $M^{3+}_{(MXene)}/M^{2+}_{(MAX)}$ and $A^{n+}_{(ACln)}/A_{(MAX)}$ redox couples as a function of temperature. (b) Assessment of thermodynamic feasibility for reactions between gaseous $SiCl_4$ and molten $ZnCl_2$ with various MAX phases at 700 °C, based on their redox potentials, for predicting reaction products. The analysis predicts that Ti_2AlC can be transformed into both a substituted MAX phase and MXene when reacting with $SiCl_4$, whereas other MAX phases (where M = V, Nb, Ta, Cr) only convert into substituted MAX phases. A similar trend is observed in reactions between M_2AlC and $ZnCl_2$, as previously reported and explained [9].

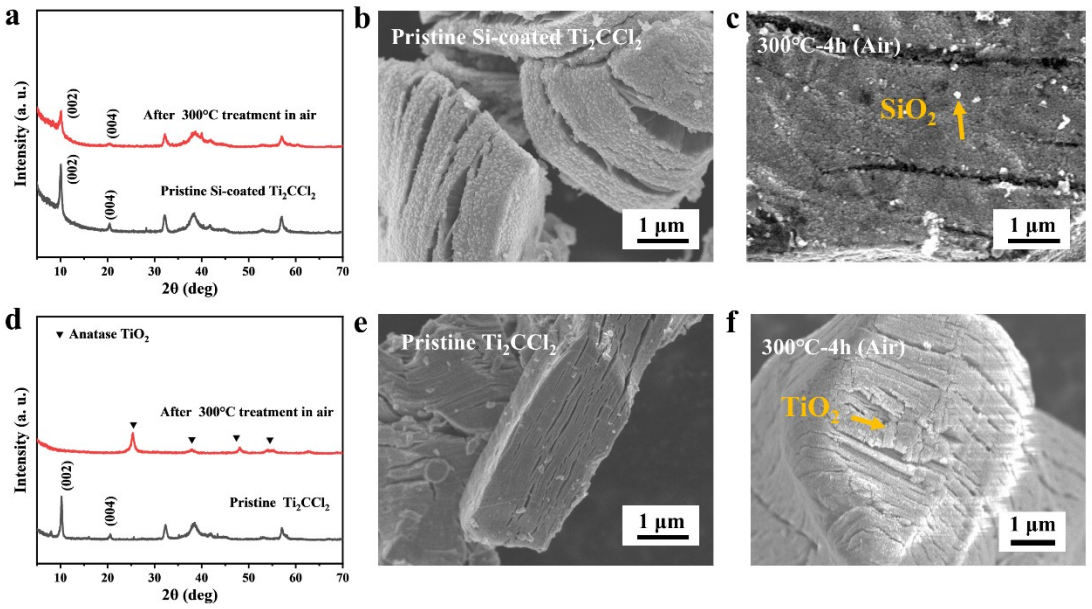

Fig. S24 Comparison of MS-Ti_2CCl_2 and Si-coated Ti_2CCl_2 before and after annealing at 300 °C in air for 4 h. (a) XRD patterns and (b, c) SEM images of Si-coated Ti_2CCl_2: (b) pristine, (c) annealed. (d) XRD patterns and (e, f) SEM images of MS- Ti_2CCl_2: (e) pristine, (f) annealed.

Reference

[1] Wang P, Mei B-c, Hong X-l, et al. Synthesis of Ti_2AlC by hot pressing and its mechanical and electrical properties. Trans. Nonferrous Met. Soc. China. 2007;17(5):1001-1004.

[2] Wu E, Herold Kisi E. Synthesis of Ti_3AlC_2 from Ti/Al_4C_3/C Studied by In Situ Neutron Diffraction. J. Am. Ceram. Soc. 2006;89(2):710-713.

[3] Lin ZJ, Zhuo MJ, Li MS, et al. Synthesis and microstructure of layered-ternary Ti_2AlN ceramic. Scr. Mater. 2007;56(12):1115-1118.

[4] Salama I, El-Raghy T, Barsoum MW. Synthesis and mechanical properties of Nb_2AlC and $(Ti,Nb)_2AlC$. J. Alloys Compd. 2002;347(1):271-278.

[5] Hu C, He L, Zhang J, et al. Microstructure and properties of bulk Ta_2AlC ceramic synthesized by an in situ reaction/hot pressing method. J. Eur. Ceram. Soc. 2008;28(8):1679-1685.

[6] Hu C, He L, Liu M, et al. In Situ Reaction Synthesis and Mechanical Properties of V_2AlC. J. Am. Ceram. Soc. 2008;91(12):4029-4035.

[7] Tian W-b, Wang P-l, Zhang G-j, et al. Mechanical Properties of Cr_2AlC Ceramics. J. Am. Ceram. Soc. 2007;90(5):1663-1666.

[8] Lin ZJ, Zhuo MJ, Zhou YC, et al. Structural characterization of a new layered-ternary Ta_4AlC_3 ceramic. Journal of Materials Research. J. Mater. Res. 2006;21(10):2587-2592.

[9] Li M, Lu J, Luo K, et al. Element Replacement Approach by Reaction with Lewis Acidic Molten Salts to Synthesize Nanolaminated MAX Phases and MXenes. J. Am. Chem. Soc. 2019;141(11):4730-4737.

[10] Li Y, Shao H, Lin Z, et al. A general Lewis acidic etching route for preparing MXenes with enhanced electrochemical performance in non-aqueous electrolyte. Nat. Mater. 2020;19(8):894-899.

[11] Mo Y, Rulis P, Ching WY. Electronic structure and optical conductivities of 20 MAX-phase compounds. Phys. Rev. B. 2012;86(16):165122.

[12] Ding H, Li Y, Li M, et al. Chemical scissor–mediated structural editing of layered transition metal carbides. Science. 2023;379(6637):1130-1135.

[13] Ghebouli MA, Ghebouli B, Fatmi M, et al. Theoretical prediction of the structural, elastic, electronic and thermal properties of the MAX phases X_2SiC (X = Ti and Cr). Intermetallics. 2011;19(12):1936-1942.

[14] Candan A, Akbudak S, Uğur Ş, et al. Theoretical research on structural, electronic, mechanical, lattice dynamical and thermodynamic properties of layered ternary nitrides Ti_2AN (A = Si, Ge and Sn). J. Alloys Compd. 2019;771:664-673.

[15] Ghebouli B, Ghebouli MA, Fatmi M, et al. First-principles calculations of structural, electronic, elastic and thermal properties of phase M_2SiC (M=Ti, V, Cr, Zr, Nb, Mo, Hf, Ta and W). Trans. Nonferrous Met. Soc. China. 2015;25(3):915-925.

[16] Amin MN, Al Faysal A, Azzouz-Rached A, et al. DFT insights into the structural, mechanical, electronic, optical, and thermal properties of Cr_2AC (A = Si, Al, Ga, Ge, and P) MAX phases carbides. AIP Adv. 2024;14(12).

[17] Islam MS, Islam AKMA. Structural, elastic, electronic and optical properties of a new layered-ternary Ta_4SiC_3 compound. Phys. B Condens. Matter.

2011;406(2):275-279.

[18] Wang XH, Zhou YC. Layered Machinable and Electrically Conductive Ti_2AlC and Ti_3AlC_2 Ceramics: a Review. J. Mater. Sci. Technol. 2010;26(5):385-416.

[19] Jeitschko W, Nowotny H, Benesovsky F. Ti_2AlN, eine stickstoffhaltige H-Phase. Monatshefte für Chemie und verwandte Teile anderer Wissenschaften. Monatsh. Chem. 1963;94(6):1198-1200.

[20] Wang H, Zhan Y, Pang M. The structure, elastic, electronic properties and Debye temperature of M_2AlC (MV, Nb and Ta) under pressure from first-principles. Comput. Mater. Sci. 2012;54:16-22.

[21] Jeitschko W, Nowotny H, Benesovsky F. Kohlenstoffhaltige ternäre Verbindungen (H-Phase). Monatsh. Chem. 1963;94(4):672-676.

[22] Bouhemadou A, Khenata R. Structural, electronic and elastic properties of M_2SC (M=Ti, Zr, Hf) compounds. Phys. Lett. A. 2008;372(42):6448-6452.

[23] Beckmann O, Boller H, Nowotny H. Neue H-Phasen. Monatsh. Chem. 1968;99(4):1580-1583.

[24] Léon A, Schild D, Fichtner M. Chemical state of Ti in sodium alanate doped with $TiCl_3$ using X-ray photoelectron spectroscopy. J. Alloys Compd. 2005;404-406:766-770.

[25] Ulgut B, Suzer S. XPS Studies of SiO_2/Si System under External Bias. Phys. Chem. B. 2003;107(13):2939-2943.